CALCULATION OF HIGH-LIFT FLOWS USING STRUCTURED AND UNSTRUCTURED GRIDS

João Alves de Oliveira Neto*, Edson Basso and João Luiz F. Azevedo****
***Instituto Tecnológico de Aeronáutica, DCTA/ITA/IEC-I,**
****Instituto de Aeronáutica e Espaço, DCTA/IAE/ALA**

Keywords: *CFD, High-lift configurations, Aerodynamic coefficients, Turbulence models*

Abstract

The purpose of the present paper is to perform a study of high-lift configurations using Computational Fluid Dynamics (CFD) simulations. Such study is an attempt to establish guidelines for the analysis and design of such devices through computational aerodynamics techniques. Structured and unstructured grids are generated for multi-element airfoils and the corresponding Reynolds-averaged Navier-Stokes (RANS) equation flow solutions are obtained around NLR 7301 and NHLP-2D geometries. As usual with RANS simulations for such high Reynolds number flows, the addition of turbulence models is required in order to capture the correct turbulent transport. In the present study, the use of the Spalart-Allmaras one-equation, Menter SST two-equation and the $k-\varepsilon$ realizable models is considered. The present effort only considers 2-D configurations, in an attempt to reduce the computational costs, and use the available grid points to explore more subtle aspects of the flow results.

1 Introduction

The design of an optimized high-lift system is an important part of the development of a modern transport aircraft. In today's highly competitive and economically driven commercial aviation market, the trend is to make aircraft systems simpler and to design and develop them faster, resulting in lower production and operational costs. Clearly, one of such systems is the high-lift system. The manufacturers must make simple, yet efficient high-lift designs and, in particular, they must avoid having to make large, expensive changes at a late project stage. The design of high-lift mechanisms is an important part of the total aircraft design process. In order to ensure acceptable performance, a large number of analyses must be performed from both the aerodynamics and mechanism standpoints. Not only do high-lift systems account for 5-11% of the total aircraft cost for a typical subsonic transport, but high-lift configuration performance is important because it can have a large impact on the total mission performance of an aircraft [1]. For example, an increase of 1% in take-off lift-to-drag ratio, $\frac{L}{D}$, for a typical long-range twin-engine subsonic transport, can result in a payload increase of 2,800 lb or a 150 nm increase in range [2]. Similarly, an increase of 1.5% in maximum lift coefficient, $C_{\ell_{max}}$, at a given approach speed can result in an additional 6,600 lb of payload [2]. These calculations reveal the potential gain from detailed high-lift system design, but the actual details of how to obtain optimal aerodynamic performance with a given high-lift system can be tedious at best. The cost and Reynolds number scaling problems involved in the optimization of slat and flap positions by wind tunnel tests is a strong driver in the effort to develop CFD tools which can be used in the design process. The paper describes one step on the road to establish CFD analysis tools for high-lift aerodynamics, by developing methods and performing validation of 2-D high-lift analysis capabilities.

High-lift flows are inherently three-dimensional and a complete study should include the modeling and analysis of such effects. However, several aspects of high-lift flows may be understood by simplified two-dimensional analysis. For instance, viscous interaction effects are responsible for the most important limiting aspects of such flows. The confluence of the wake of one element with the suction side boundary layer of the following elements plays an important role in determining maximum lift. Massive flow separation on one or more of the elements may, depending on operational condition, set the maximum lift which can be obtained. The fact that many portions of the flow develop in strong adverse pressure gradient regions increases the modeling difficulties. The knowledge of turbulence development in adverse pressure gradient regions is much less developed than it is for zero pressure gradient flows. Most turbulence models used in Reynolds averaged computational methods are calibrated in zero pressure gradient flows, with more or less *ad hoc* modifications to account for the development of turbulence in adverse pressure gradient regions. Moreover, many effects in high-lift flows are governed by the detailed transition process. This can be quite different in wind tunnel tests taken at lower Reynolds number compared to the flight situation. The numerical calculation of all of these phenomena must also address the subjects of grid refinement and grid independent solutions. In any event, even with the known limitations of 2-D analysis in mind, the results are still quite useful in the initial design phase and to increase the understanding of the governing flow phenomena.

In this context, the purpose of the present work is to perform a systematic analysis of several physical and numerical aspects which can influence the quality of simulations of high-lift flows. The first aspect to be addressed concerns the fundamental question in numerical calculations associated with grid refinement and its effects on the flow solution obtained. Mesh independent results may be difficult to achieve, especially for such complex flows as usually found in high-lift systems. The paper will also address the effect of turbulence models on the quality of the high-lift solutions. The present effort will only consider 2-D configurations, in an attempt to reduce the computational costs, and use the available mesh points to explore more subtle aspects of the 2-D results.

As previously discussed, difficulties for creating a CFD capability for high-lift systems are inherent both to the geometric complexity of multi-element airfoils as well as to the limitations in flow physics modeling. Flowfields over high-lift systems are characterized by highly complex flow physics, which pose significant challenges for CFD codes. The list of relevant flow physics issues includes laminar flow, transition, attachment line transition, relaminarization, confluent boundary layers, wake interactions, separation, and reattachment. It is, then, clear that viscous flow techniques are necessary to accurately predict the characteristics of high-lift configurations. Likewise, as the flow contains both compressible and incompressible zones simultaneously, the use of a compressible Navier-Stokes code is preferable [1]. The current trend is towards a more efficient, yet simpler design that will lead to reduced manufacturing and maintenance costs. At the same time, increases in lift coefficients for a given angle of attack, increases in maximum lift coefficients and in lift-to-drag ratios will lead to a larger payload capability.

For this purpose, results for some high-lift configurations are obtained using a CFD code currently under development by the group and these results are compared to data available in the literature and/or computations also performed by the authors using well-established commercial codes. The study looks into 2-D configurations, under high-lift conditions, and it assesses the capability of predicting lift, drag and pressure coefficients for such configurations. The present CFD tool is a finite volume code for unstructured 3-D meshes, which uses a fully explicit, 2nd-order, 5-stage Runge-Kutta scheme to perform the time march of the Reynolds-averaged Navier-Stokes (RANS) equations. A scheme for the flux calculation at the volume faces is implemented

and the scheme is based on Roe's flux difference splitting method [3]. The implementation uses a cell-centered, face-based data structure and the code can use meshes composed of any combination of tetrahedra, hexahedra, triangular-based prisms and square-based pyramids. As usual with RANS simulations for such high Reynolds number flows, the addition of turbulence models is required in order to capture the correct turbulent transport. In the present case, the use of both the Spalart-Allmaras (SA) one-equation, Menter SST (SST) two-equation and the realizable k-ε models is considered.

This introduction section describes the motivation for the current effort. In the second section of this paper, the theoretical and numerical formulations embedded in the numerical tool are briefly presented. In the third section, a summary of the currently considered linear eddy-viscosity turbulence models is presented. A careful evaluation of numerical simulation results is presented in the fourth section. Finally, a concluding remark section closes the paper with the major conclusions obtained from the current effort.

2 Theoretical and Numerical Formulations

2.1 Reynolds-Averaged Navier-Stokes Equations

The formulation implemented in the CFD code currently under development by the group [4] considers the 3-D compressible Reynolds-averaged Navier-Stokes (RANS) equations, written in dimensionless form and assuming a perfect gas, as

$$\frac{\partial \mathbf{Q}}{\partial t} + \nabla \cdot (\mathbf{P}_e - \mathbf{P}_v) = 0 \,, \tag{1}$$

where $\mathbf{Q}$ is the vector of conserved variables, defined as

$$Q = \left[\begin{array}{cccccc} \rho & \rho u & \rho v & \rho w & e \end{array} \right]^T . \tag{2}$$

The inviscid and viscous flux vectors are given as

$$\mathbf{P}_e = \left\{ \begin{array}{c} \rho \upsilon \\ \rho u \upsilon + p\hat{\beta}_x \\ \rho v \upsilon + p\hat{\beta}_y \\ \rho w \upsilon + p\hat{\beta}_z \\ (e+p)\upsilon \end{array} \right\} , \mathbf{P}_v = \frac{1}{Re} \left\{ \begin{array}{c} 0 \\ (\tau^{\ell}_{xi} + \tau^{t}_{xi})\hat{i}_i \\ (\tau^{\ell}_{yi} + \tau^{t}_{yi})\hat{i}_i \\ (\tau^{\ell}_{zi} + \tau^{t}_{zi})\hat{i}_i \\ \beta_i \hat{i}_i \end{array} \right\} . \tag{3}$$

The shear-stress tensor is defined by

$$\tau^{\ell}_{ij} = \mu_{\ell} \left[\left(\frac{\partial u_i}{\partial x_j} + \frac{\partial u_j}{\partial x_i} \right) - \frac{2}{3} \frac{\partial u_m}{\partial x_m} \delta_{ij} \right] , \tag{4}$$

where u_i are the Cartesian velocity components and x_i are the Cartesian coordinates. The viscous force work and heat transfer term, β_i, is defined as $\beta_i = \tau_{ij} u_j - q_j$, where the heat transfer component is defined as

$$q_j = -\gamma \left(\frac{\mu_{\ell}}{Pr} + \frac{\mu_t}{Pr_t} \right) \frac{\partial (e_i)}{\partial x_j} \,. \tag{5}$$

It is important to remark that, for the flow conditions of interest here, the Reynolds analogy for the turbulent heat transfer, as considered in Eq. 5, is adequate and numerically robust. The molecular dynamic viscosity coefficient, μ_{ℓ}, is computed by Shutherland law [5]. The dimensionless pressure can be calculated from the perfect gas equation of state.

2.2 Finite Volume Discretization

The finite volume method is used to obtain the solution of the RANS equations. The formulation of the method is obtained by an integration of the flow equations (Eq. 1) in a discrete volume. The application of Gauss theorem for each finite volume yields

$$\int_{Vi} \frac{\partial \mathbf{Q}}{\partial t} dV + \int_{Si} (\mathbf{P}_e - \mathbf{P}_v) \cdot d\mathbf{S} = 0 \,, \tag{6}$$

where the outward-oriented area vector is defined as

$$\mathbf{S} = (S_x, S_y, S_z) \,. \tag{7}$$

The discrete value of the vector of conserved variables in the i-th control volume is defined as

the mean value of the conserved variables in the volume. This definition can be written as

$$\mathbf{Q}_i = \frac{1}{V_i}\int_{Vi} \mathbf{Q} dV_i \ . \tag{8}$$

Hence, the final form of the finite volume formulation for the RANS equations is obtained for an elementary volume, and assuming a stationary mesh, as

$$\frac{\partial \mathbf{Q}_i}{\partial t} = -\frac{1}{V_i}\sum_{k=1}^{nf}(\mathbf{P}_{e_k} - \mathbf{P}_{v_k})\cdot \mathbf{S}_k \ , \tag{9}$$

where the k subscript indicates properties computed in the k-th face, and nf is the number of faces which form the i-th control volume. This equation indicates that the integral discretized assuming the fluxes to be constant on the faces, which is a sufficient approximation for obtaining 2nd-order accuracy in space for the currently available flux computation schemes. The code is able to handle grids composed of cells of the tetrahedron, hexahedron, wedge, or pyramid types, or a mix of these types of elements.

2.3 Time Integration

The integration in time of Eq. 9 is currently performed using a fully explicit, 5-stage, 2nd-order in time, Runge-Kutta type scheme [6, 7]

$$\begin{aligned} \mathbf{Q}_i^{(0)} &= \mathbf{Q}_i^n \quad , \\ \mathbf{Q}_i^{(\ell)} &= \mathbf{Q}_i^{(0)} - \frac{\alpha_\ell \Delta t_i}{V_i}\mathbf{RHS}_i^{l-1} \ , \\ \mathbf{Q}_i^{n+1} &= \mathbf{Q}_i^{(5)} \quad . \end{aligned} \tag{10}$$

with the α_ℓ coefficients defined as 1/4, 1/6, 3/8, 1/2 and 1 for $\ell = 1,...,5$, respectively [6]. The residue , **RHS**, is here defined as

$$\mathbf{RHS}_i = \mathbf{C}_i - \mathbf{V}_i - \mathbf{D}_i, \tag{11}$$

where $\mathbf{C}_i$, $\mathbf{V}_i$ and $\mathbf{D}_i$ are, respectively, the convective, the viscous, and the artificial dissipation operators, calculated for the i-th control volume. These operators are computed according to the adopted spatial discretization scheme. In order to save computational resources for viscous flow simulations, the viscous operator is calculated only in the first stage of the Runga-Kutta scheme [6]. Reference [6] shows that this operation is successful in reducing computational costs while consistently maintaining the same quality of results when computing the viscous terms at all stages. Similarly, the artificial dissipation term, when applicable, is computed in the first, third and fifth stages of the Runge-Kutta scheme for viscous flows, and in the first and second stages for the inviscid cases.

2.4 Spatial Discretization

The upwind discretization in the present context is performed by the Roe flux-difference splitting method [3]. For this scheme, the inviscid convective flux is defined as

$$\mathbf{C}_i = \sum_{k=1}^{nf}\mathbf{P}_{e_k}\cdot\mathbf{S}_k \ , \tag{12}$$

where the numerical flux in the k-th face is

$$\begin{aligned} \mathbf{P}_{e_k}\cdot\mathbf{S}_k &= \frac{1}{2}\left[\mathbf{P}_e(\mathbf{Q}_L) + \mathbf{P}_e(\mathbf{Q}_R)\right]\cdot\mathbf{S}_k \\ &- \frac{1}{2}\left|\tilde{\mathbf{A}}_\mathbf{k}\right|(\mathbf{Q}_R - \mathbf{Q}_L)\left|\mathbf{S}_k\right| \ , \end{aligned} \tag{13}$$

and $|\tilde{\mathbf{A}}_\mathbf{k}|$ is the Roe matrix associated with the k-th face normal direction, computed by

$$\left|\tilde{\mathbf{A}}_\mathbf{k}\right|(\mathbf{Q}_R - \mathbf{Q}_L) = \sum_{j=1}^{5}|\lambda_j|\delta_j\mathbf{r_j} \ . \tag{14}$$

In this formulation, $|\lambda_j|$ represents the magnitude of the eigenvalues associated with the Euler equations, given as

$$|\Lambda| = diag(|\upsilon_n|, |\upsilon_n|, |\upsilon_n|, |\upsilon_n + a|, |\upsilon_n - a|) \ . \tag{15}$$

Similarly, $\mathbf{r_j}$ represents the associated eigenvectors and the δ_j terms represent the projections of the property jumps at the interface over the system eigenvectors, defined as the elements of

$$\Delta = \mathbf{L}\left[\begin{array}{ccccc}\delta(\rho) & \delta(\rho u) & \delta(\rho v) & \delta(\rho w) & \delta(e)\end{array}\right]^T \ , \tag{16}$$

where $\delta()$ represents the jump of the property in the interfaces as $\delta() = ()_R - ()_L$, and the left

eigenvectors are the rows of the **L** matrix. In the various definitions presented before, the k-th subscript, that indicates a variable computed in the face, is eliminated in order to avoid overloading the equations with symbols. More details on the theoretical and numerical formulations can be found in Refs. [8] and [9].

3 Turbulence Modeling

Engineering applications of fluid dynamics may be divided into two groups regarding the turbulence effects [4]. For one group, turbulence may be neglected and common numerical results are adequate to obtain good accuracy. For the second group, turbulent effects are an essential feature for the flow configuration, and numerical simulations will show a dependency on the details of turbulence models used. Typical external flows of interest for aeronautical industries certainly fall into the latter group. Usually, high-Reynolds number flows are considered, and complicated phenomena such as boundary layer and shock wave interactions, adverse pressure effects, flow separation, wing wakes, mixing layers, and others, surely occur. Thus, the inclusion of turbulence effects into the present computational tool is of paramount importance for accurate predictions of such flow conditions. The turbulence effects are included into the RANS equations by the Reynolds-stress tensor, defined by

$$\tau_{ij}^{t} = -Re\overline{\rho u_i'' u_j''} \, . \tag{17}$$

Various turbulence models are available in the current code, ranging from linear and non-linear eddy-viscosity models, to Reynolds-stress models. The model transport equations are also solved according to the finite volume approach. In the present work, however, only three eddy-viscosity models are actually used, and brief comments on such models are presented in the forthcoming subsections. It should also be pointed out that eddy-viscosity turbulence models compute the Reynolds stresses (Eq. 17) through the Boussinesq hypothesis, which states that the turbulence stresses are a linear function of the mean flow straining rate times a modifying constant, such as

$$\tau_{ij}^{t} = 2\mu_t S_{ij} - \frac{2}{3}\rho k \delta_{ij}, \tag{18}$$

$$S_{ij} = \frac{1}{2}\left(\frac{\partial u_i}{\partial x_j} + \frac{\partial u_j}{\partial x_i}\right) - \frac{1}{3}\frac{\partial u_m}{\partial x_m}\delta_{ij} \, , \tag{19}$$

where μ_t is the eddy-viscosity coefficient computed by the chosen turbulence model.

3.1 Spalart-Allmaras Model

The Spalart-Allamaras one-equation model [10] solves a transport equation for a modified eddy-viscosity coefficient. Its transport equation can be integrated to the wall without any numerical difficulty provided that $y^+ \approx 1$ near the wall. The model is derived along intuitive, empirical lines, heavily relying on calibration by reference to a wide range of experimental data and on the knowledge of the distance to the wall. The model has been applied without any further modification by the CFD community for 3-D compressible flows with good results for shock-induced separations and adverse-pressure gradient boundary layers [11, 12]. Since this model does not make use of the turbulent kinetic energy, k, the last term in Eq. 18 is assumed to be zero.

3.2 Shear-Stress Transport Model

Further improvement on the high-Reynolds-number Wilcox $k-\omega$ model can be obtained with the Menter SST model [13, 14]. The SST model is derived from a blend of the original $k-\omega$ [15] and the standard $k-\varepsilon$ [16] models. It solves reported problems of the $k-\omega$ closure regarding freestream value dependency [14] while keeping the better numerical behavior of this model close to the wall. Model constants are generally calculated as $\phi = F_1\phi_1 + (1-F_1)\phi_2$, where ϕ_1 represents the set of constants for the $k-\omega$ model and ϕ_2 represents the set for the standard $k-\varepsilon$ model, as in Ref. [14]. The F_1 variable is a blending function that turns on the $k-\omega$ closure near solid walls and the standard $k-\varepsilon$ model outside boundary layers, and it is dependent on the distance to the wall.

It is known in the CFD community that standard two-equation models are not capable of accurately computing adverse-pressure gradients or separated flows [13]. These models require a stronger pressure gradient or a longer running length to separate than it is indicated by experiments. It is demonstrated that this is a result of the missing effect of turbulent shear-stress transport in this type of flow [17]. In order to take the shear stress into account, at least in an *ad hoc* fashion, the eddy-viscosity coefficient for the SST model is bounded by a measure of the flow strain rate [14]. Another blending function is used to turn on this criterion only inside boundary layers. A careful discussion on the motivations for this procedure can be found in Ref. [13]. A simpler version of the SST model, denoted the BSL model [13], exactly follows the above formulation, but without the last criterion for the eddy-viscosity coefficient [13]. Both BSL and SST models can be integrated to the wall when $y^+ \approx 1$ near the wall.

3.3 Realizable k–ε Model

The realizable $k-\varepsilon$ (RKE) model [18] solves transport equations for k and ε. A realizable estimate of the turbulent time scale, based on the local turbulent Reynolds number, removes the stiffness of the original $k-\varepsilon$ model [16] near solid walls. An additional term in the dissipation-rate equation is considered to improve the model response to adverse-pressure gradient regions. The eddy-viscosity coefficient is bounded following a Schwarz inequality realizability criterion [18]. In that definition, a low-Reynolds-number damping function, designed to account for the damping of turbulent fluctuations near solid walls, is also available. These features compose a model that does not require the distance to the wall and that can be integrated through the whole boundary layer provided that $y^+ \approx 1$ near the wall.

4 Results and Discussion

In the present paper, results for two high-lift configurations (NLR 7301 airfoil and NHLP-2D airfoil) are obtained. The study will look into 2-D configurations, under high-lift conditions, and assess the capability of predicting lift, drag and pressure coefficients for such configurations.

4.1 NLR 7301 Airfoil

The NLR 7301 is a supercritical airfoil/flap configuration with 32% chord flap. This geometry, considering a $\delta_f = 20^o$ flap deflection and with a 1.3% gap [19], is shown in Fig. 1. The gap is defined as the radius of the circumference centered at the trailing edge of the main element and tangent to the flap profile at a certain point. This point of tangency is defined by the overhang, which is held at a constant value of 5.3% for test case here considered. It is worth mentioning that the gap and the overhang are defined as a percentage of the nominal profile cruise chord. Simulations of subsonic flow over the NLR 7301 profile are performed with freestream Mach number $M_\infty = 0.185$ and Re = 2.51 x 10^6, considering viscous flow options.

Fig. 1 Enlarged view of the NLR 7301 airfoil.

The present paper contemplates the study of numerical results including lift and drag coefficients for the NLR 7301 airfoil with 1.3% gap, and the comparison with experimental data. At the present work, approximately 72 test cases have been considered so far, that is, two gap values, with three turbulence models, and five different angle of attacks have been calculated. In the present analysis, three unstructured meshes with different refinements are used. These meshes are denoted initial, medium and final meshes. These meshes have rectangular topologies and the external boundary is located at 100 chord lengths from the profile. To assure good quality in all meshes, unstructured grids composed of hexahedra have been generated. Details of the grids used in the simulations can be seen in the Tab. 1.

Table 1 Details of computational grids used for the NLR 7301 airfoil simulations with 1.3% gap.

Grid	Initial	Medium	Final
Elements total	156.731	382.997	866.391

The initial grid used for the aerodynamic calculation has a total of 156,731 elements. Simulations of subsonic flow over the NLR 7301 profile are performed with freestream Mach number $M_\infty = 0.185$ and Re = 2.51 x 10^6, considering viscous formulation. In these simulations, both SA, SST and $k-\varepsilon$ realizable turbulence models are exercised, as a form of comparing their results. The lift coefficient as a function of the angle of attack can be observed, in details, in the Fig. 2, that in this case that it were calculated with the initial grid. This figures compares the turbulence

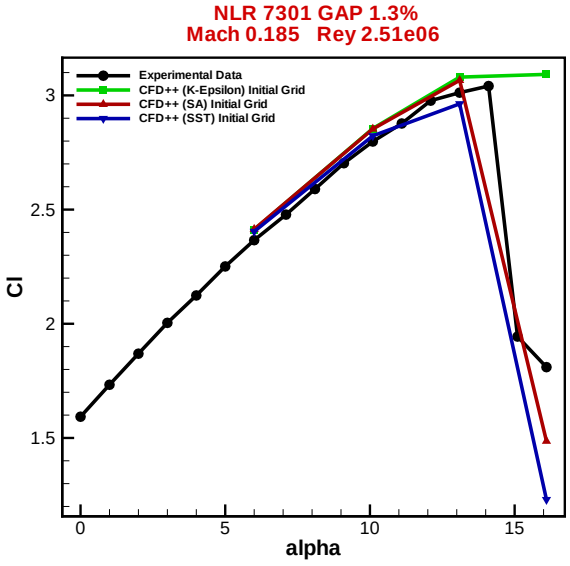

Fig. 2 The lift coefficient as a function of the angle of attack with Mach number 0.185 for the NLR 7301 with 1.3% gap using initial grid.

models presented in that analysis with the experimental data. It is possible observe that the SA and SST turbulence models also shows a good result in comparison with the experimental results. Already the $k-\varepsilon$ turbulence model achievable not obtain a good agreement in the nonlinear region of the flow in question.

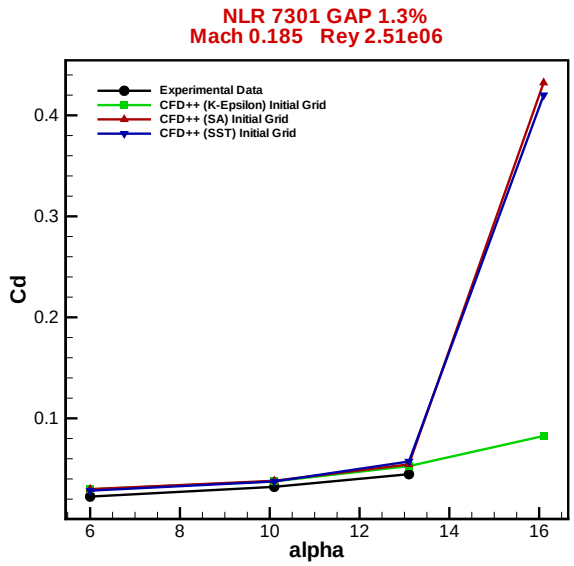

Fig. 3 The drag coefficient as a function of the angle of attack with Mach number 0.185 for the NLR 7301 with 1.3% gap using initial grid.

In Fig. 3, is possible observe the drag coefficient as a function of the angle of attack, computed with the initial grid. In the linear region of the drag coefficient curve, the results with the SA and SST turbulence models presented a good result, including in the nonlinear region. Unfortunately, the $k-\varepsilon$ realizable turbulence model did not behave as expected in the region of high angle of attack. In the reality, this incapacity of the $k-\varepsilon$ realizable model achievable of do a forecast of the separation of the flow is associated to the absence of answer to the curvature of the flow.

To second grid utilized for the calculation of the aerodynamic coefficients has a total of 382.997 elements. Once again, simulations of subsonic flow over the NLR 7301 profile are performed with freestream Mach number $M_\infty =$ 0.185 and Re = 2.51 x 10^6, considering viscous formulation. In these simulations, both SA, SST and $k-\varepsilon$ realizable turbulence models are exercised, as a form of comparing their results. The lift coefficient as a function of the angle of attack

can be observed in detail in the Fig. 4. In This figures, the SA turbulence model overestimates the curve of Cl versus alpha of the experimental result, but the calculation of Cl obtained convergence. In case of the SST model, the calculation of the lift coefficient, when the angle of attack is 12.1^o was not satisfactory, therefore the value of Cl not obtain convergence. Beyond this, the value of the $k-\varepsilon$ turbulence model achievable not obtain good agreement with the experimental results, ignoring the region of not linearity near to the region of the stall.

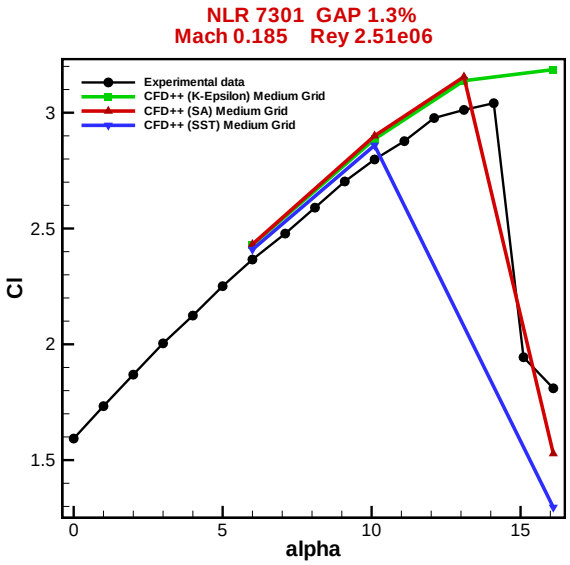

Fig. 4 The lift coefficient as a function of the angle of attack with Mach number 0.185 for the NLR 7301 with 1.3% gap using medium grid.

In Fig. 5 is possible observe the drag coefficient as a function of the angle of attack, computed with the medium grid. In the linear region of the drag coefficient curve, the results with the SA and SST turbulence models presented a good result, including in the nonlinear regions, unless, in case of 12.1^o the angle of attack the value of the drag coefficient not obtain convergence in case of of the calculation with the SST model.

Unfortunately, the $k-\varepsilon$ realizable turbulence model achievable did not calculate as expected the drag coefficient in the region of high angle of

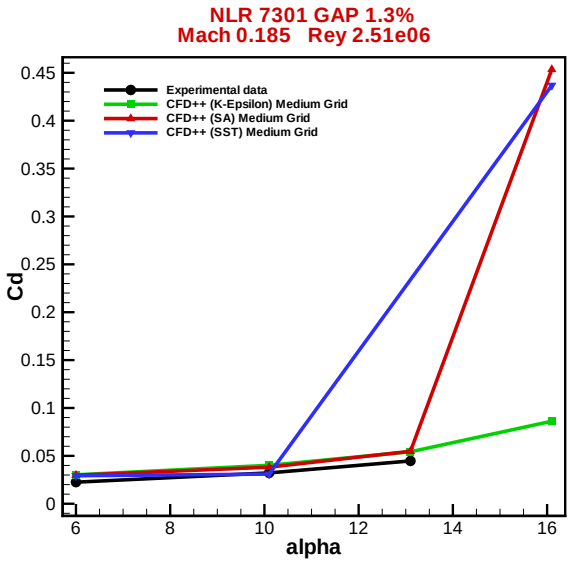

Fig. 5 The drag coefficient as a function of the angle of attack with Mach number 0.185 for the NLR 7301 with 1.3% gap using medium grid.

attack. Once again, this deficiency of the $k-\varepsilon$ model achievable, of do a forecast of the detachment of the flow, is associated to the absence of answer to the curvature of the flow.

The third grid utilized for the calculation of the aerodynamic coefficients has a total of 866.391 volumes of control. Like this, the simulations are carried out with the freestream Mach number of 0.185 and Reynolds number of Re = 2.51 x 10^6 utilizing a formulation RANS. The curve Cl x α can be observed in details in the Fig. 6. Verifying this figure, the SA, SST and $k-\varepsilon$ tubulence models achievable overestimate the curve Cl x α of the experimental result. In case of the $k-\varepsilon$ model achievable, the calculation of the lift coefficient of when the angle of attack was of 6^o and 16.1^o, respectively, was not satisfactory, therefore the value of lift coefficient diverged in those values of α.

In Fig. 7, is possible observe the drag coefficient as a function of the angle of attack, computed with the final grid. In the linear region of the drag coefficient curve, the results with all of the models of turbulence presented a good agreement including in the nonlinear region. Once

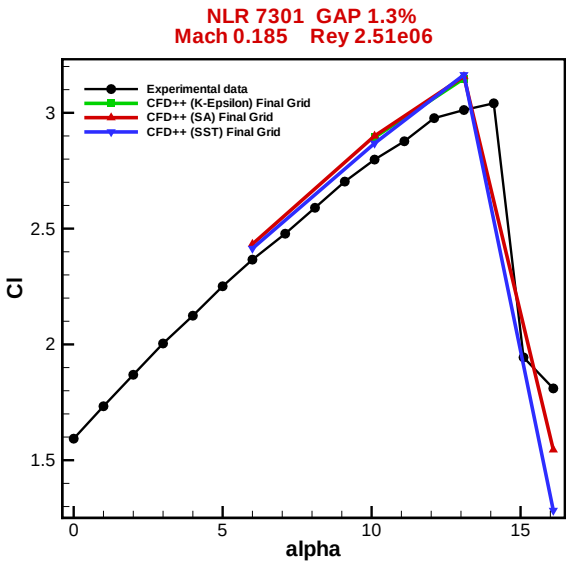

Fig. 6 The lift coefficient as a function of the angle of attack with Mach number 0.185 for the NLR 7301 with 1.3% gap using final grid.

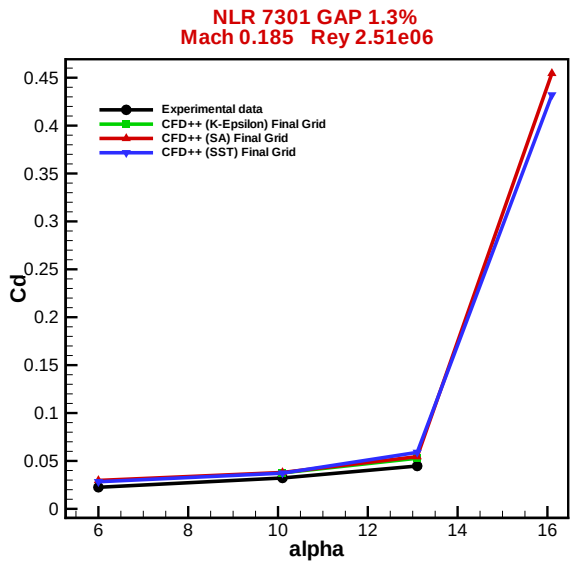

Fig. 7 The drag coefficient as a function of the angle of attack with Mach number 0.185 for the NLR 7301 with 1.3% gap using final grid.

again, had problem for the calculations in 6^o and 16.1^o of the angles of attack. In these cases, the calculation of the coefficient diverged for the $k-\varepsilon$ turbulence model achievable. Being like this, the $k-\varepsilon$ model achievable did not calculate as expected the drag coefficient in the region of high angle of attack.

4.2 NHLP-2D Airfoil

Wind tunnel data were measured for a two-dimensional supercritical airfoil with high-lift devices and the model designation is NHLP-2D [21]. The case selected for examination here is L1T2 which includes a 12.5%c leading-edge slat and a 33%c single slotted-flap, where c is the chord length of the nested configuration. The slat is located in the optimum position at an angle of 25 degrees and the flap angle is 20 degrees. This geometry, which is typical of a take-off configuration, is show in Fig. 8. The flow conditions for this case are freestream Mach number $M_\infty =$ 0.197 and Re = 3.52 x 10^6, and an angle of attack of 4^o, considering both inviscid and viscous flow options. In these simulations, both SA and SST turbulence models are exercised, as a form of comparing their results. In the present simulations, quadrilateral mesh is used with 148.014 elements. Locations along the chord in which total pressure profiles are indicated in Fig. 8.

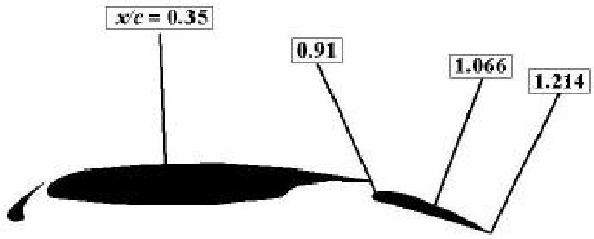

Fig. 8 Location of stations for which total pressure profiles are shown for the NHLP-2D airfoil.

The numerical results obtained by Morrison [22], using the Wilcox $k-\omega$ turbulence model, are also presented together with experimental data [21] for total pressure profile comparisons. The plot for x/c = 0.35, presented in Fig. 9, shows the slat wake and the boundary layer on the main

element. The experimental data is sparse in the region of the slat wake and shows a narrower and weaker wake when compared to numerical results. The results of Morrison [22] predict a slat wake which is too large. The experiment shows more merging of the slat wake and main element boundary layer than the calculations show. There are differences in the two models, but they all fundamentally show a more distinct and boundary layer than the experimental.

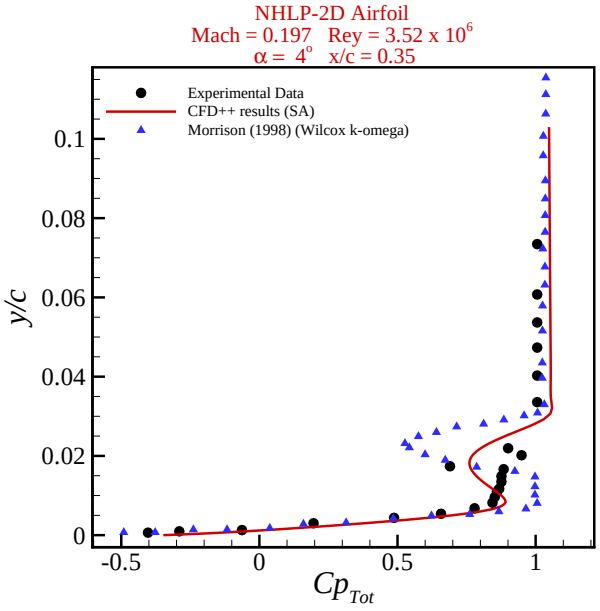

Fig. 9 Total pressure profile at x/c = 0.35 for the NHLP-2D three element airfoil.

The experimental profiles at all of the other downstream locations confirm the merging of the slat wake with element boundary layer, the slat wake is completely missing from the experimental total pressure profiles at the x/c = 0.91 and higher locations, presented in Fig. 10. All two of the models predict a distinct slat wake in the outer edge of the main element boundary layer all the way to the flap trailing edge (x/c = 1.214), described in Fig. 12. The SA turbulence model shows the smallest wake at all the stations and the $k-\omega$ model shows the largest wake at all of the locations. The wake location is predicted very similarly for SA turbulence model, but the wake defect and wake width vary.

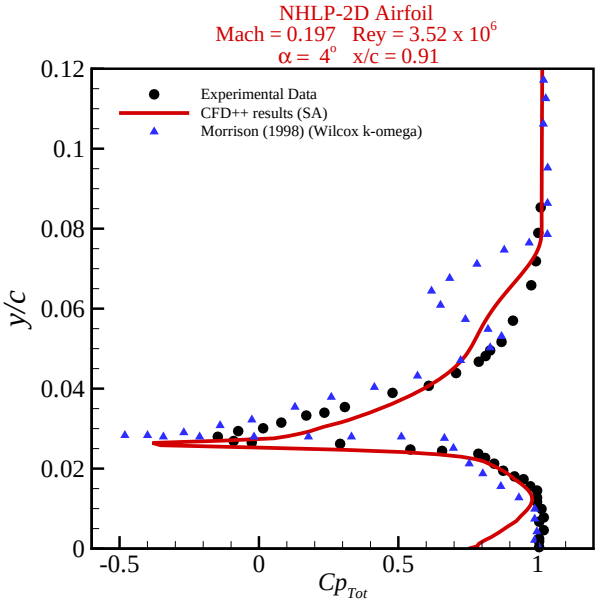

Fig. 10 Total pressure profile at x/c = 0.91 for the NHLP-2D three element airfoil.

5 Conclusion

In this paper, simulation results for 2-D high-lift configurations obtained with SA, SST and realizable $k-\varepsilon$ turbulence models are presented. Two geometries are considered, namely the NLR 7301 airfoil and the NHLP-2D airfoil. For such configurations, the paper compares the results obtained using the three different turbulence models in terms of the relevant parameters for high-lift aerodynamic flows. The SA turbulence model is more accurate in attached flows and wakes, including merging boundary layers and wakes. Considering the uncertainties associated with the experimental data and the use RANS approximation, the performance of these SA and SST turbulence models is very good for the present applications. The SA turbulence model is preferred for general, mostly attached aerodynamic flows, whereas the SST turbulence model seems to be the best choice if separated flows are of primary interest. The present calculations also present good agreement with data available in the literature.

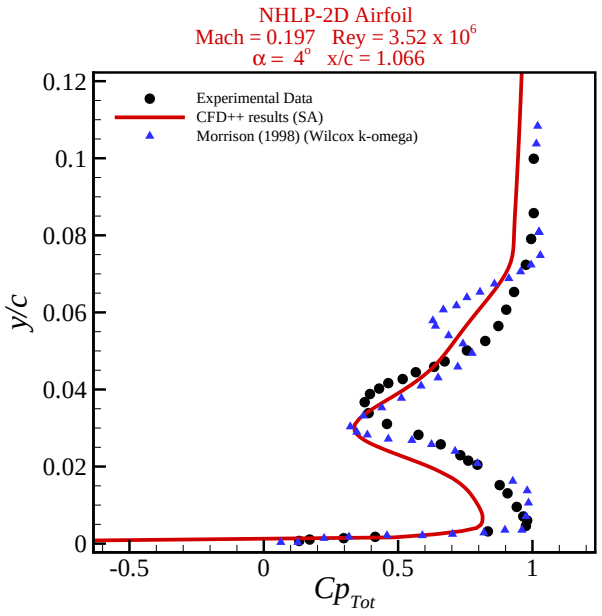

Fig. 11 Total pressure profile at x/c = 1.066 for the NHLP-2D three element airfoil.

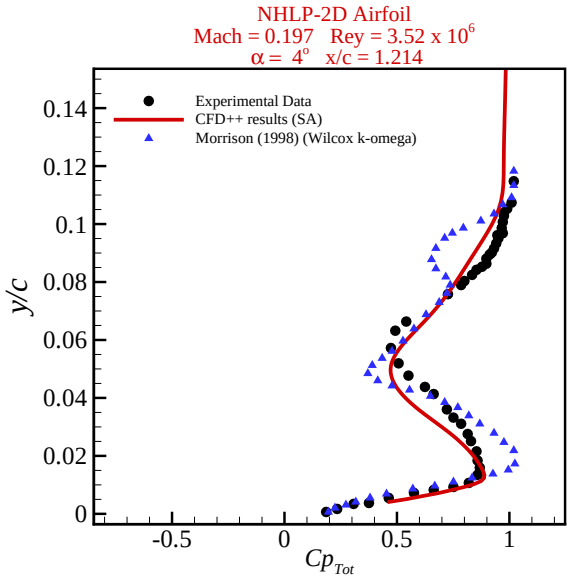

Fig. 12 Total pressure profile at x/c = 1.214 for the NHLP-2D three element airfoil.

6 Acknowledgments

The authors gratefully acknowledge the support of Fundação de Amparo à Pesquisa do Estado de São Paulo (FAPESP) through a Master's Scholarship for the first author under the FAPESP Grant No. 05/57867-0. The authors also acknowledge the partial support of Conselho Nacional de Desenvolvimento Científico e Tecnológico, CNPq, through the Integrated Project Research Grant No. 312064/2006-3.

References

[1] van Dam, C. P., "The Aerodynamic Design of Multi-Element High-Lift Systems for Transport Airplanes," *Progress Aerospace Sciences*, Vol. 38, 2002, pp. 101-144.

[2] Meredith, P. T., "Viscous Phenomena Affecting High-Lift Systems and Suggestions for Future CFD Development," High-Lift System Aerodynamics, AGARD CP-315, pp. 19-1 to 19-8.

[3] Roe, P. L., "Approximate Riemann Solvers, Parameter Vectors, and Difference Schemes," *Journal of Computational Physics*, Vol. 43, No. 2, 1981, pp. 200-212.

[4] Bigarella, E. D. V., *"Advanced Turbulence Modelling for Complex Aerospace Applications,"*PhD Thesis, Instituto Tecnológico de Aeronáutica, São José dos Campos, SP, Brazil, 2007.

[5] Anderson, Jr. J. D., *"Fundamentals of Aerodynamics,"* 2nd ed., McGraw-Hill, New York, 1991.

[6] Jameson, A., Schmidt, W., and Turkel, E., "Numerical Solutions of the Euler Equations by Finite Volume Methods Using Runge-Kutta Time-Stepping Schemes," *AIAA Paper No. 81-1259, Proceedings of the 14th AIAA Fluid and Plasma Dynamics Conference*, Palo Alto, CA, 1981, pp. 1-17.

[7] Jameson, A., and Mavriplis, D. J., "Finite Volume Solution of the Two-Dimensional Euler Equations on a Regular Triangular Mesh," *AIAA Journal*, Vol. 24, No. 4, 1986, pp. 611-618.

[8] Scalabrin, L. C., *"Numerical Simulation of Three-Dimensional Flows over Aerospace Configurations,"* Master's Thesis, Instituto Tecnológico de Aeronáutica, São José dos Campos, SP, Brazil, 2002.

[9] Bigarella, E. D. V., and Azevedo, J. L. F., "A Study of Convective Flux Computation

Schemes for Aerodynamic Flows," AIAA Paper 2005-0633, 2005.

[10] Spalart, P. R., and Allmaras, S. R., "A One-Equation Turbulence Model for Aerodynamic Flow," *La Recherche Aeropastiale*, Vol. 01, 1994, pp. 5-21.

[11] Leschziner, M. A., and Drikakis, D., "Turbulence Modelling and Turbulent-Flow Computation in Aeronautics," *The Aeronautical Journal*, Vol. 106, No. 1061, 2002, pp. 349-383.

[12] Spalart, P. R., "Strategies for Turbulence Modelling and Simulations," *International Journal of Heat and Fluid Flow*, Vol. 21, No. 3, 2000, pp. 252-263.

[13] Menter, F. R., "Zonal Two-Equation $k-\omega$ Turbulence Models for Aerodynamic Flows," AIAA Paper 93-2906, 1993.

[14] Menter, F. R., "Two-Equation Eddy-Viscosity Turbulence Models for Engineering Applications," *AIAA Journal*, Vol. 32, No. 8, 1994, pp. 1598-1605.

[15] Wilcox, D. C., *"Turbulence Modeling for CFD,"* 2nd ed., DCW Industries, La Canada, CA, 1998.

[16] Jones, W. P., and Launder, B. E., "The Prediction of Laminarization with a Two-Equation Model of Turbulence," *International Journal of Heat and Mass Transfer*, Vol. 15, No. 2, 1972, pp. 301-314.

[17] Johnson, D. A., and King, L. S., "A Mathematically Simple Turbulence Closure Model for Attached and Separated Turbulent Boundary Layers," *AIAA Journal*, Vol. 23, No. 11, 1985, pp. 1684-1692.

[18] Shih, T., Liou, W. W., Shabbir, A., Yang, Z., and Zhu, J., "A New Eddy Viscosity Model for High Reynolds Number Turbulent Flows: Development and Validation," NASA TM-106721, Aug. 1994.

[19] van den Berg, B., and Gooden, J. H. M., "Low Speed Surface Pressure and Boundary Layer Measurement Data for the NLR 7301 Airfoil Section with Trailing Edge Flap," A Selection of Experimental Test Cases for the Validation of CFD Codes, AGARD AR-303, Vol. 2, 1994.

[20] Lima-Silva, A. L. F., Oliveira Neto, J. A., Antunes, A. P., Mendonça, M. T., and Azevedo, J. L. F., and Silveira Neto, A., "Numerical Study of Two-Dimensional High-Lift Configurations Using the MSES Code," *Proceedings of the 18th International Congress of Mechanical Engineering, COBEM 2005*, Ouro Preto, MG, Brazil, 2005.

[21] Moir, I. R. M., "Measurements on a Two-Dimensional Aerofoil with High-Lift Devices," A Selection of Experimental Test Cases for the Validation of CFD Codes, AGARD AR-303, Vol. 2, 1994.

[22] Morrison, J. H., "Numerical Study of Turbulence Model Predictions for the MD 30P/30N and NHLP-2D Three-Element High-Lift Configurations," NASA CR-1998-208967, 1998.

Copyright Statement